Density Derivation Using Controlled Spacecraft Potential in Earth's Magnetosheath and Multi-scale Fluctuation Analysis

D. Teubenbacher[1], O. W. Roberts[1], R. Nakamura[1], Y. Narita[1], Z. Vörös[1], K. Torkar[1], P.-A. Lindqvist[2], R. E. Ergun[3]

[1]Space Research Institute, Austrian Academy of Sciences, Graz, Austria
[2]Division of Space and Plasma Physics, Royal Institute of Technology, SE-100 44 Stockholm, Sweden
[3]Laboratory for Atmospheric and Space Physics, University of Colorado, Boulder, CO 80303 USA

Key Points:

- High time resolution electron density is derived from spacecraft potential on MMS during operation of the ion emitters.
- Multi-point magnetic field and the derived electron density data are used to investigate compressive turbulent fluctuations in the magnetosheath.
- The presented analysis and technique are significant for studying physical processes in space plasmas ranging from fluid to kinetic scales.

Corresponding author: Daniel Teubenbacher, `daniel.teubenbacher@oeaw.ac.at`

Abstract

In-situ measurements from the Magnetospheric Multiscale (MMS) mission are used to estimate electron density from spacecraft potential and investigate compressive turbulence in the Earth's magnetosheath. During the MMS Solar Wind Turbulence Campaign in February 2019, the four MMS spacecraft were arranged in a logarithmic line constellation enabling the study of measurements from multiple spacecraft at varying distances. We estimate the electron density from spacecraft potential for a time interval in which the ion emitters actively control the potential. The derived electron density data product has a higher temporal resolution than the plasma instruments, enabling the examination of fluctuation for scales down to the sub-ion range. The inter-spacecraft separations range from 132 km to 916 km; this corresponds to scales of 3.5 to 24.1 ion inertial lengths. The derived density and magnetic field data are used to study fluctuations in the magnetosheath through time lags on a single spacecraft and spatial lags between pairs of spacecraft over almost one decade in scale. The results show an increase in anisotropy as the scale decreases.

1 Introduction

Space plasmas often exhibit large-amplitude, nearly randomly-fluctuating turbulent motions. The solar wind and planetary magnetosheaths are good examples of turbulent plasmas, also showing a varying level of compressibility in terms of magnetic field magnitude and particle number density (Bruno & Carbone, 2013).As the solar wind plasma expands to the interplanetary space, instead of the expected fast adiabatic cooling, the temperature profile shows a more moderate decrease with heliospheric distance (Williams et al., 1995; Borovsky & Gary, 2014; Perrone et al., 2019). Turbulent dissipation can act through many channels such as wave-particle interactions or through dissipation in coherent structures which are intermittently distributed in space (Osman et al., 2012; Wu et al., 2013). Intermittency (Kolmogorov, 1941; Frisch, 1995; Matthaeus et al., 2015) is an indication of the existence of coherent structures, meaning structures that have longer lifetimes than the ambient stochastic fluctuations (Bruno, 2019).

In contrast to a neutral fluid, a strong magnetic field causes the turbulence to be anisotropic, with different components of the magnetic field having different powers, i.e., variance/power anisotropy (Matthaeus et al., 2005; Oughton et al., 2015). The fluctuations in a plasma become elongated along the mean magnetic field direction so that wavevectors in the perpendicular direction $k_\perp$ dominate the parallel direction $k_\parallel$ ($k_\perp \gg k_\parallel$), i.e., there is wavevector anisotropy (Narita et al., 2011; Roberts et al., 2013, 2015). To investigate anisotropy with a single spacecraft, different intervals are investigated where the mean magnetic field direction is at different orientations with respect to the sampling direction (bulk velocity). However, this involves comparing different intervals. Ideally, to have a better understanding of kinetic scale plasma turbulence, multi-point measurements (to resolve the spatio-temporal ambiguity) with high temporal cadence (to resolve kinetic-scale fluctuations) have to be analyzed (Klein et al., 2019).

In the Earth's magnetosheath turbulence is different from the solar wind in terms of showing larger fluctuation amplitudes presumably coming from shock amplification and also a higher level of compressibility. In general, magnetosheath plasma is hotter and denser and the mean magnetic field is stronger than in the solar wind (Alexandrova (2008)). This complex process makes the magnetosheath an interesting plasma region for turbulence studies.

In February 2019, the Magnetospheric MultiScale (MMS) Solar Wind Turbulence Campaign was conducted (Burch et al., 2016; Garner, 2019; Bandyopadhyay et al., 2020; Chasapis et al., 2020). During the three-week campaign, the apogee (toward Sun) was raised to about 27 R_E which enabled long intervals in the pristine solar wind, without magnetic connection to the foreshock. Additionally, the configuration of the four spacecraft was changed from a regular tetrahedron to a "logarithmic line" constellation. The inter-spacecraft distances span from about 25 to 200 km at apogee with the overall baseline being almost perpendicular to the solar wind bulk velocity direction at apogee. Having measurements from spacecraft at varying distances results in poor directional coverage as the baseline angles are almost the same for each spacecraft pairing. However, it allows the investigation of turbulent fluctuations over a larger range of spatial scales.

In this study, data from this campaign are used to study the statistical properties of (derived) electron density and magnetic field fluctuations in the Earth's magnetosheath. We first derive the electron density data from spacecraft potential measurements. During the time interval the Active Spacecraft Potential Control (ASPOC) instrument was controlling the spacecraft potential which requires a derivation scheme including the ion emitter current, the validation and statistical analysis of the electron density data. We then investigate the statistical properties of the magnetosheath plasma on the inbound portion of the orbit where the inter-spacecraft distances ranged between 132 km and 916 km to perform multi-scale analysis.

The paper is structured as follows: Section 2 presents the MMS data and describes the derivation of the electron density from spacecraft potential measurements, Section 3 shows the validation and statistical analysis of the electron density data. A discussion and summary in Section 4 concludes the paper.

2 MMS Spacecraft Potential as Density Estimator

The following MMS fast survey mode data are used (sampling rates in brackets) in this study: the ion current from ASPOC I_{ASPOC} (1 Hz) (Torkar et al., 2016), the spacecraft potential V_{sc} from Spin Double Probe (SDP 32 Hz) (Lindqvist et al., 2016), the electron temperature T_e and density n_e from the Fast Plasma Investigation instrument (FPI, 0.22Hz) (Pollock et al., 2016), the spin phase data from SDP (32 Hz) as well as the magnetic field data from fluxgate magnetometer FGM (16 Hz) (Russell et al., 2016). Fig. 1 shows measurements from the MMS1 spacecraft in the time period from February 26^{th} 2019 13:00 UTC to 17:00 UTC. During this interval the ASPOC instrument was operating, resulting in a controlled spacecraft potential. The ion currents on MMS2, MMS3, and MMS4 were almost constant throughout the time window, the second ASPOC emitter on MMS1 shows a dip of the ion current for a few minutes at about 16:20 of $\sim 14\,\%$ which is due to an instability in the beam.

One aim of this work was to make use of the spacecraft potential data in fast survey mode (Baker et al., 2016) at a resolution of 32 Hz to obtain electron plasma density data. In this way, the time resolution of the density data can be improved by a factor of 144 from 0.22 Hz to 32 Hz in comparison to measurements by FPI (Pollock et al. (2016)). The method used here is based on the works by Pedersen (1995), Andriopoulou et al. (2015), Torkar et al. (2015) and Nakagawa et al. (2000) and utilizes the spacecraft potential measurements and plasma moments in order to derive the electron density at high resolution. The potential calibration technique has been used for uncontrolled spacecraft potential in the past (Pedersen et al. (1984); Pedersen (1995); Pedersen et al. (2001, 2008)). Several studies also discussed the calibration when the potential was actively controlled by an ion emitter like the ASPOC instrument (Torkar et al. (2019); Andriopoulou et al. (2015); Andriopoulou et al. (2016); Andriopoulou et al. (2018)). While these reports showed some limited examples to demonstrate the method using spin-resolution data, it is the first time that this method is applied for higher-resolution data which requires some refinements removing the spin data in addition to the inclusion of the ion current from ASPOC in the derivation scheme. Furthermore, we used the derived data for analysis.

Figure 1. Measurements from the MMS1 spacecraft on February 26th, 2019 from 13:00 UTC to 17:00 UTC. The panels, from top to bottom represent: Electric field and magnetic field in GSE coordinates (Fränz & Harper, 2002), an omnidirectional electron energy spectrum, spacecraft potential, ASPOC ion current, electron temperature, number density of electrons and ions.

In the uncontrolled case, the current balance equation of a spacecraft in a tenuous plasma is governed by the thermal electron current collected by the spacecraft I_e and the photoelectron current $I_{\rm phot}$ leaving the spacecraft. The ASPOC instruments can be used to prevent spacecraft charging greater than +4 V by emitting ions to give a current $I_{\rm ASPOC}$. Other currents can contribute to the current balance but, in general, are much smaller (Torkar et al., 2019). The secondary electron emission is not always small. It depends on surface material properties as well as incident electron energy. For most materials, the peak of secondary electron emission is at around 300 - 800 eV, meaning that if the incident electron current has a temperature outside this range, the number of secondary electrons emitted is low (Balcon et al., 2011), which is the case for this study. Accordingly, the following balance equation can be used when ASPOC controls the spacecraft potential:

$$I_{\rm e} + I_{\rm phot} + I_{\rm ASPOC} = 0 \tag{1}$$

Assuming a Maxwellian distribution of the particle velocities, the thermal electron current I_e (Mott-Smith & Langmuir, 1926) can be expressed as

$$I_e = -A_{sc}|q|n_e\sqrt{\frac{k_{\rm B}T_e}{2m_e\pi}}c \tag{2}$$

where T_e is the electron temperature, q is the electron charge, m_e is the electron mass, n_e is the electron density, $k_{\rm B}$ Boltzmann's constant and $c = (1 + (qV_{sc}/k_{\rm B}T_e))$ a correction factor that accounts for the surplus of electrons that is attracted due to a positively charged spacecraft (Torkar et al., 2019). V_{sc} is the spacecraft potential and $A_{sc} = 34\ m^2$ is the effective surface area of the MMS spacecraft.

If the energy of the incoming solar radiation and exact surface material properties are known, the photoelectron current that is leaving the spacecraft can be calculated. In addition, the area of the sunlit part of the spacecraft has to be known at every point of time, which is especially difficult for a spinning spacecraft (Pedersen, 1995). Consequently, another method to determine $I_{\rm phot}$ is used here. It employs the simplified current balance equation (Eq. 1) and the floating spacecraft potential, which is established where the current balance is given. The photoelectron current is modeled using a combination of one or more exponential terms, each having a current and a potential coefficient (Pedersen, 1995; Torkar et al., 2019; Andriopoulou et al., 2015). The number of exponential terms depends on the number of photoelectron populations. In previous studies, the usage of two (Torkar et al., 2019; Nakamura et al., 2017) or three (Andriopoulou et al., 2015) exponential terms has proven to be sufficient. In this work, the approximation with two exponential functions was used as there is one photoelectron population with a higher current at lower energy and the other population with a lower current at a higher energy. The model function can be written as:

$$I_{\rm phot} = I_{01}e^{-V_{sc}/V_{01}} + I_{02}e^{-V_{sc}/V_{02}} \tag{3}$$

with I_{01} and I_{02} as current coefficients (current units) and V_{01} and V_{02} as potential coefficients (potential units) related to the characteristic energy of the respective photoelectron population (Andriopoulou et al., 2016).

For using data with a time resolution higher than the spin period, 20 s (0.05 Hz), the effect from the spin needs to be removed since the spacecraft rotation causes a constant change in the sunlit area and the photoelectron emission and creates a variation in spacecraft potential data not due to the change in the ambient electrons. The spin effect can be seen as spikes in the Fourier spectra of the potential measurements (Yao et al., 2011; Roberts et al., 2017). To remove the spin effect, the spin phase data along with the spacecraft potential fluctuations are used to develop an empirical spin model for each of the four MMS spacecraft (Roberts et al., 2017) (Roberts et al., 2020). Using a non-linear least-squares fit (Markwardt, 2009) with ten sine curves, the spin effect of each spacecraft can be subtracted from the spacecraft potential data, leading to a spin-tone removed V_{sc} that is used to derive the average photoelectron curve as well as the electron density.

With the spin tone removed spacecraft potential data V_{sc} and the ASPOC ion current I_{ASPOC}, there is only one parameter missing to derive an average photoelectron curve in the simplified current balance model (Eq. 1). It is the thermal electron current I_e, and it can be calculated using FPI measurements (see Eq. 2). All data are re-sampled to 4.5 s cadence, which is the time resolution of fast mode data of the FPI measurements. The photoelectron current $I_{phot} = I_e + I_{ASPOC}$ can be plotted against the spacecraft potential, see Fig. 2. In this figure, the data points (grey dots) are binned into 100 equally spaced potential bins, and the mean value of data points within each bin is then displayed as a black star. The error bars represent the standard deviations of the mean bin values to the rest of the data points in each bin. The model function with two exponential functions (Eq. 3) is fitted to the data (green curve). This model function is the average photoelectron curve needed to derive electron densities from spacecraft potential data as in Eq. (4).

When looking at the data points in Fig. 2, one can see that there are two "clouds", one between 2.5 V and 3.0 V and the second one between 4.0 V and 4.8 V. Looking at those potential ranges in Fig. 1, it can be seen that cloud 2 corresponds to the time interval between 13:00 UTC and 14:00 UTC where electron temperatures were two magnitudes higher than in the time after 14:00 UTC, which can be identified as cloud 1. The region of interest for further analysis is the time period in the magnetosheath (14:20 to 17:00 UTC), and therefore, electron temperatures are averaged over this period to $T_{e,avg} = 33\,eV$. In order to derive the electron density at 32 Hz, the ASPOC ion current is interpolated using cubic splines to match the data rate. This is reasonable as the ASPOC current only shows variations of about 1 %.

Finally, by rearranging the current balance equation Eq. (1), the thermal electron current (Eq. 2) and the modeled photoelectron current, the electron density can explicitely be estimated as follows:

$$n_e = \frac{1}{A_{sc}|q|}\sqrt{\frac{2\pi m_e}{kT_e}}\frac{1}{1+\frac{qV_{sc}}{k_B T_e}} \cdot \left[\left(I_{01}e^{-V_{sc}/V_{01}} + I_{02}e^{-V_{sc}/V_{02}}\right) + I_{ASPOC}\right] \qquad (4)$$

where n_e is the derived electron density, V_{sc} is the spacecraft potential and $A_{sc} = 34\,m^2$ is the effective spacecraft surface area.

A direct comparison of the measured and derived electron densities is shown in Fig. 3. The panel in the middle shows the normalized difference $Err(n_e) = (n_{e,der} - n_{e,meas})/n_{e,meas}$ between the two densities. In the time before 14:20, $Err(n_e)$ is mostly above 100%; this is due to the assumption made about the electron temperature. In general, one can see that $Err(n_e)$ and also its variation is high (± 40 %) in the time period from 13:50 UTC to 14:10 UTC. These variations might be caused by to stronger electric fields (see Fig. 1 panel 1) and thereby caused perturbations in the spacecraft potential due to enhanced photoelectron emission when the electric field distorts the potential in the sheath around the spacecraft. The influence of strong ambient electric fields on spacecraft potential measurements was shown by Torkar et al. (2017); Graham et al. (2018); Roberts et al. (2020). The focus of the further analysis is on the time interval after the transition into the magnetosheath region, where the electric field strength components are rather small ($< 4\,mV/m$). In the time period from 14:10 - 17:00, the normalized difference decreases to a small value, $Err(n_e) = -5\%$ on average.

The electron densities derived from the other three MMS spacecraft show qualitatively the same results. For MMS4, several assumptions had to be made due to the lack of electron plasma data from FPI. First of all, the electron temperature of MMS1

Figure 2. MMS1 average photoelectron curve: grey dots represent data points, black stars the mean of those data points within 100 equally spaced potential bins (with standard deviations as error bars) and the green graph is the two exponential model fit for the photoelectron curve with the four coefficients written in green.

was used to compute the average photoelectron curve. The average $T_e = 33$ eV is then used for calculation. Secondly, the ion density measurement from MMS4 was used instead of the electron density. The use of ion density is reasonable, and the estimation compares well (of the order of a few percent) with the three other spacecraft.

3 Validation of the Electron Density Data and Application to Turbulence Analysis

The derived density data will be validated using the - lower resolution - FPI data sets as a comparison. We then analyze characteristics of fluctuations in both the magnetic field and in electron density and compare by performing statistical analysis. As the electron density is a scalar we do not need to consider a coordinate system. However, for the magnetic field a physically relevant coordinate system should be considered for the comparison. We perform a coordinate transform based on the mean magnetic field direction. The measured data are available in the geocentric solar ecliptic (GSE) coordinate system, and are transformed into a parallel and two arbitrarily chosen perpendicular magnetic field components:

$$\vec{B}_{parallel}(t) = B_x(t) \cdot B_{0,x} + B_y(t) \cdot B_{0,y} + B_z(t) \cdot B_{0,z} \tag{5}$$

$$\vec{B}_{perp1}(t) = B_x(t) \cdot e_{\perp 1,x} + B_y(t) \cdot e_{\perp 1,y} + B_z(t) \cdot e_{\perp 1,z} \tag{6}$$

$$\vec{B}_{perp2}(t) = B_x(t) \cdot e_{\perp 2,x} + B_y(t) \cdot e_{\perp 2,y} + B_z(t) \cdot e_{\perp 2,z} \tag{7}$$

where $\hat{\vec{B}}_0$ is the mean magnetic field direction unit vector, $\vec{B}_{parallel}$ points in the mean field direction and $\vec{B}_{\perp 1}$ and $\vec{B}_{\perp 2}$ are the two perpendicular directions in the coordinate system. $\hat{\vec{e}}_{\perp 1} = \hat{\vec{B}}_0 \times (1,\ 0,\ 0)$ is the first perpendicular vector and the second one is $\hat{\vec{e}}_{\perp 2} = \frac{\hat{\vec{B}}_0 \times \vec{e}_{\perp 1}}{|\hat{\vec{B}}_0 \times \vec{e}_{\perp 1}|}$.

This coordinate transform can be justified as if the magnetic field direction is relatively stable in chosen time interval (see Fig. 3). The parallel magnetic field component represents the compressive component and can qualitatively be compared to the density fluctuations. Similar work was done in Roberts et al. (2022) where it is also discussed why the definition of a mean magnetic field is a sensitive issue (Oughton & Matthaeus, 2020).

In order to validate the potential calibration, a smaller sub-interval was selected that complies with the following two requirements:

1. The difference of measured and derived electron densities is below 5 % on average.
2. The statistical analysis of the magnetic field will be performed in global mean magnetic field coordinates, therefore the direction of the magnetic field should not vary more than 5°in the interval so that a mean magnetic field direction is well defined.

The challenge is to find a period that fulfils both requirements while being as long as possible at the same time. The shorter the time series is, the greater the uncertainty will be in determining structure functions (e.g. Dudok de Wit et al. (2013)) especially at higher orders, or large scales. The following figure, Fig. 3 shows both, the comparison of the derived and measured (FPI) electron density as well as the magnetic field measurements (FGM, Russell et al. (2016)) of the MMS1 probe for the whole time interval from 13:00 to 17:00 on February 26^{th} 2019. When looking only at the magnetosheath period from about 14:20 to 17:00 UTC, the longest time period where the magnetic field does not change its direction substantially, is between 15:00 UTC and 15:40 UTC. The average relative difference between measured and derived electron density is with -3% relatively small. We therefore used data from this time period (15:00 UTC to 15:40 UTC) for further analysis.

We investigate the statistical properties of the fluctuations using the following two methods. The first method calculates fluctuations from a variable (magnetic field or electron density in our case) using time lags and data from only one spacecraft (Eq. 8).

$$\Delta B_{t,\tau} = B(t+\tau) - B(t) \tag{8}$$

The scale of the fluctuations is defined by the timescale τ. The second method uses different combinations of two spacecraft; a fluctuation is defined with a spatial lag as seen in Eq. 9.

$$\Delta B_{a,b}(t) = B_a(t) - B_b(t) \tag{9}$$

A time lag can be converted to a spatial distance along the flow direction using the ion bulk speed, i.e., Taylor's frozen-in flow hypothesis (Taylor, 1938). This approximation assumes that the fluctuation evolves slowly compared to the time taken for it to advect over the measurement point. The conversion of a time lag in this manner allows spatial lags in different directions (along the bulk flow and along the spacecraft separation direction) to be calculated. The novel spacecraft formation allows the comparison of temporal and spatial lags over a larger range of scales than possible with a tetrahedron (e.g., Chhiber et al. (2018) and Chasapis et al. (2017)).

To quantify the power of the fluctuations in different directions we calculate the second order structure functions (p=2) which are generally defined in Eq. 10.

$$D^{(p)} \equiv \langle |\Delta B|^p \rangle \tag{10}$$

Where ΔB is calculated from time lags e.g. Eq 8 or spatial lags Eq 12 and the angled brackets denote an average. Higher orders of structure functions can give insight into properties such as the intermittency. However, we focus here on the second order structure function, as higher orders are more susceptible to outliers especially during shorter time intervals e.g. (K. Kiyani et al., 2006)

When using single spacecraft time lagged measurements; the second order structure function at a time τ is defined as;

$$D^{(p)}(\tau) \equiv \langle |\Delta B_\tau|^p \rangle \tag{11}$$

Time lags can be converted to a spatial lag along the stream direction assuming Taylor's hypothesis $\tau = \lambda / v_b$, with v_b being the mean ion bulk speed and λ being the spatial lag. If there are measurements available from multiple satellites available such as with MMS, it is also possible to look at the spatial variation of a measurement directly by comparing measurements at the same times at different spatial locations. If they are in the bulk flow direction, comparing single spacecraft time lagged variations with multi-spacecraft spatial lag variations using the solar wind speed as proportionality factor, the validity of Taylor's hypothesis can be evaluated (Bruno & Carbone, 2013).

In the multi-spacecraft case, the increments are defined as the difference between the measurements of two spacecraft a, b at the same time t. The structure function can then be calculated as:

$$D^{(p)}_{ab}(\lambda) \equiv \langle |\, (B_a(t) - B_b(t))\, |^p \rangle \tag{12}$$

Time lagged structure functions, where the timescale is converted to a spatial scale can then be compared directly to the spatially lagged measurements.

Figure 3. MMS1 Multipanel Plot from 26-02-2019. The panels, from top to bottom represent: number density of electrons measured from FPI (red) and derived with the spacecraft potential (black), and the relative difference between the measured and derived electron densities and the magnetic field measurements from FGM in GSE coordinates. The grey area marks the selected time interval for statistical analysis.

In the chosen time period from 15:00-15:40 UTC, the minimum separation between two MMS spacecraft is 132 km (MMS1-MMS4) and the maximum distance is 916 km (MMS2-MMS3). The average magnetic field strength $\langle B \rangle$ is 13.7 nT and the root-mean-square magnetic fluctuation weighted by the average magnetic field is $\delta B/\langle \vec{B} \rangle = \sqrt{\langle |\vec{B}(t) - \langle \vec{B} \rangle|^2 \rangle}/\langle \vec{B} \rangle = 0.377$. The average electron plasma density $\langle n_e \rangle$ is 35 cm^{-3} and the ion and electron inertial lengths are $d_i = 38$ km and $d_e = 1$ km. The ion plasma beta that describes the ratio of thermal to magnetic pressure is $\beta_i = \frac{nk_B T_i}{B^2/2\mu_0} = 10$. Finally, the mean Alfvén speed is $v_A = 50$ km/s and the mean flow speed $v_B = 138$ km/s.

The mean magnetic field direction during the selected time interval can be calculated by averaging the components $\vec{B}_{mean} = [\langle B_x(t) \rangle, \langle B_y(t) \rangle, \langle B_z(t) \rangle]$. Normalizing leads to the unit vector $\hat{\vec{B}}_0 = (0.14, -0.17, -0.97)$. It can be seen that the magnetic field mostly points in the negative z-direction, this is illustrated in Fig. 4, together with the mean flow direction and the spacecraft positions in the XY-, XZ- and YZ-plane. One perpendicular direction can be found as cross product of the mean field direction $\hat{\vec{B}}_0$ with the unit vector in X-direction, the second perpendicular direction is then the cross product of $\hat{\vec{B}}_0$ with the first perpendicular direction. The angle between mean magnetic field direction and mean flow direction is 111° and the angle between the mean magnetic field direction and the respective spacecraft baselines is 85°. It can be seen that the spacecraft baselines are parallel and measure almost perpendicular to the mean magnetic field. The (common) baseline direction is also the movement direction of the satellites on their orbit in this logarithmic line constellation.

The statistical analysis can now be performed for both, the derived electron density as well as on the magnetic field measurement in mean field coordinates. The smallest time lag used is the time interval between two consecutive measurements, which is $\tau_{mag,min} = 0.063$ sec for the magnetic field measurements as the time resolution of the FGM instrument is 16 Hz in fast survey mode. For the electron density, the smallest time lag is $\tau_{den,min} = 0.032$ sec corresponding to 32 Hz. The largest time lag is chosen to be $\tau_{max} = 100$ sec, which is about 45% of the whole 40-min time interval. Using Eq. 10 and 12, one can compute the structure functions of order $p = 2$ of the individual magnetic field components as well as the electron density as function of time lag τ. While the structure functions can be plotted directly, another way of analyzing the second-order structure function implies the so-called *equivalent spectrum* $S^{(2)} \equiv D^{(2)}\lambda$. Together with the effective wave number $k^* \equiv 1/\lambda$, $S^{(2)}$ shows a similar behavior as a Fourier spectrum and can therefore be used to estimate spectral slopes (see e.g. Chhiber et al. (2018))

In Fig. 5, panel (a) the equivalent spectrum for the magnetic field is shown. The time-lagged structure functions are indicated by the solid lines, with the dotted lines representing the parallel and perpendicular magnetic field components and the solid black line is the so called trace magnetic field structure function. At large scales, the equivalent spectrum of the magnetic field follows the 1/f regime (K. H. Kiyani et al., 2015). The inertial range with a scaling exponent of -5/3 is also denoted, however, there seems to be a rather direct transition from the 1/f region to a steeper slope with a scaling exponent of -8/3, which is consistent to previous studies like Czaykowska et al. (2001), Alexandrova (2008), Chhiber et al. (2018), Macek et al. (2018). The steepening occurs at about four times the ion gyro radius $4 \cdot \rho_i \sim 500$ km (Note: $d_i = 38km$ and $rho_i = 122km$, so $d_i + \rho_i = 160km$ which means that the steepening occurs at about three times $(d_i + rho_i)$).

The six symbols in Fig.5 denote structure functions of the six unique two-spacecraft pairs. The pairing "14" for instance means the spatial separation from MMS1 to MMS4, the others are "12", "13", "23", "34", "24". It is important to note that the often used term "spatial lag" actually describes the spatial separation between the spacecraft averaged over the time interval. Moreover, the analysis of MMS1 data is representative for

Figure 4. Mean positions of the four MMS spacecraft on February 26^{th}, 2019: 15:00-15:40 in GSE coordinates. (a): XY-plane, (b): XZ-plane, (c): YZ-plane. The mean magnetic field direction $\vec{B}_0$ (black) and the mean flow direction $\mathbf{V}_{SW}$ (red) are scaled up for visualisation.

the other spacecraft as the variations between the different single-spacecraft structure functions are negligible.

It can be seen that the power of increments of the parallel (compressive) component of the magnetic field is higher than the power of the perpendicular components (see Fig. 5, panel (a)). Moreover, it is evident that there is in general a good agreement between the power of the multi-spacecraft measurements and the time-lagged measurements. However, it is important to note that the time-lagged measurements are obtained in flow direction, whereas the spatial-lagged measurements are taken in spacecraft baseline direction. This directional difference of the increments can be used to investigate the anisotropy by looking at the difference of the structure functions. The ratio of the spatial-lagged and nearest neighbor time-lagged measurement can be seen in panel (b) of Fig. 5. They are in general close to unity in the range of inter-spacecraft separations of 132 km to 916 km, or in units of the ion inertial length 3.5 d_i to 24 d_i. Nevertheless, the multi-spacecraft measurements show a consistently higher power than the single-spacecraft measurements ($D_{\mathrm{single}}/D_{\mathrm{multi}} < 1$). Additionally, there seems to be a trend of increasingly smaller ratios for smaller and smaller lags. As the time-lagged structure functions indicate fluctuations in a different direction than the spatially-lagged structure functions, this enhanced derivation from 1 suggests higher anisotropy at smaller scales.

The equivalent spectrum for the derived electron plasma density can be seen in Fig. 5 panel (c). The electron density fluctuations represent the compressive part directly and can therefore quantitatively be compared with the compressive fluctuations of the magnetic field. In general, the scaling observed for the electron density is very similar in comparison with the magnetic field analysis. Only at large scales, the electron density equivalent spectrum seems to be steeper by a few percent. Additionally, there is good agreement between the power of the multi-spacecraft measurements. This can be checked by looking at the ratio of the structure functions plotted in panel (d). A trend of increasingly smaller ratios for smaller and smaller lags that seen in the magnetic field analysis cannot be observed clearly here.

4 Discussion

The electron plasma density derivation scheme (Andriopoulou et al., 2015; Andriopoulou et al., 2016; Andriopoulou et al., 2018; Torkar et al., 2019) is applied to a magnetopause crossing an magnetosheath interval on Feb. 26, 13:00-17:00 UT. The results are validated with MMS FPI measurements. The derived density data showed only a few percent difference to the interpolated plasma measurements. The methods enabled to obtain densities at much higher time resolution for the magnetosheath interval on Feb. 26, 2019, from 14:00 to 17:00 UT. There seems to be a trend of an underestimation of the electron density in the last two hours of the time interval of about 9 % on average, which may be due to assuming an average electron temperature $T_e = 33$ eV within the total magnetosheath period.

The short interval with the dip of the ASPOC ion current of one emitter on MMS1 of max. 20 % from 16:15-16:25 UT (see Fig. 1) does not have any notable influence on the density derivation, since the ambient electron current dominates over the total ASPOC ion current for this particular interval. One may, however, need to more carefully select the interval with a stable ASPOC beam for other sparse plasma regions when applying this method.

We found that even if assuming that the MMS probes are in a very similar plasma environment, an average photoelectron curve modelled from one spacecraft cannot be used for density derivations on other MMS spacecraft without significant deviations from the FPI measurements (Andriopoulou et al., 2018). Hence, an average photoelectron curve was computed for each of the MMS spacecraft for the whole time interval from 13:00 UTC

Figure 5. Statistical analysis: Second-order (p=2) structure functions of the mean magnetic field components and combined trace magnetic field (normalized, panel (a)) and electron density (panel c) as equivalent spectrum $S^{(2)}$. The X-Axis is units of the inverse spatial lag λ and is called effective wave number k^* (k^* is not identical to the wave number k of the regular frequency spectrum). Graphs denote MMS1 single spacecraft (time-lag) and symbols the multi-spacecraft (spatial-lag) structure functions (six different MMS combinations denoted by numbers in the legend). d_i is the ion inertial length and ρ_i the ion gyro radius. Three spectral slopes at the scaling exponents of -1, -5/3 and -8/3 are plotted in grey as a reference. Panels (b) and (d) show the ratios of structure functions of the trace magnetic field and electron density from single and multi-spacecraft measurements. The ratio is obtained using the spatial lag measurement and the nearest neighbor time-lagged measurement that is converted into a spatial lag λ using the ion bulk velocity.

to 17:00 UTC, 26^{th} of February 2019. Including also the transition region from magnetopause to magnetosheath (right before 14:00) enabled to have a larger range of potential values from 1.9 V to 5.8 V.

For the statistical analysis we selected a time interval that is long enough to make higher-order statistics reasonable and when the magnetic field direction was rather stable to obtain a well defined mean field. Although finding such an interval in the magnetosheath was challenging we could select a 40 min time interval that had sufficient measurement data of both, the magnetic field and the electron density to compute structure functions of order two. While the equivalent spectrum for the electron density is slightly steeper at large scales ($k^* < 10^{-3}\,\mathrm{km}^{-1}$), both equivalent spectra displayed in panels (a) and (c) in Fig. 5 show similar scaling laws. It can be observed that there is only a short or even no inertial range (-5/3 slope), instead there is a direct transition from the (1/f) range to he steeper (-8/3) region. This is consistent with findings of studies done by Chasapis et al. (2017), Chhiber et al. (2018) and Roberts et al. (2020). The compressive magnetic field component shows a consistently higher power than the transverse components.

In previous studies employing multi-spacecraft measurements, like the ones mentioned above, the inter-spacecraft distances were much smaller for each spacecraft pairing, and the constellation arranged in a tetrahedron. A comparison of time-lagged and spatially-lagged was therefore limited to a small spatial range. In this study, the logarithmic line constellation of the MMS spacecraft enabled comparison over almost one decade in scale as demonstrated in Fig. 5. Nevertheless it is important to mention that it was not accounted for the angle between the flow direction (time-lagged measurements) and the spacecraft baselines (spatially-lagged measurements). To verify Taylor's Hypothesis, meaning that the ratio of the structure functions is unity, the spacecraft baseline directions and the flow direction need to be the same. Contrarily, if the goal is to find anisotropies, these directions need to be different. In this case, however, it is not possible to fully verify Taylor's Hypothesis. Yet, the detail comparisons between the measurements over the wide range of scales suggested some differences in the anisotropy.

The statistics of the electron density show in general very similar behavior in comparison to the magnetic field. Despite the fact that the derived electron density shows good results in comparison to the FPI measurements one needs caution to compare point-to-point derived density data of multiple spacecraft as noise and systematic errors might be induced into the measurements. Further details on that issue can be found in Andriopoulou et al. (2015).

5 Conclusions

Data obtained from the MMS Solar Wind Turbulence Campaign from February 26, 2019, provided a great data base to use density proxy data derived from the spacecraft potential for studying turbulence in the Earth's magnetosheath.

In this study we derive the electron density for each of the MMS satellites during a period when the ASPOC instrument was operating and the spacecraft potential was actively controlled. By also removing the spin tone in the spacecraft potential data, plasma density with a much higher time resolution than the measurements from the MMS plasma instruments (FPI) was derived. On average, the derived density is 3 % lower than the FPI measurements in the relevant magnetosheath time interval, which means there is a slight underestimation of the derived density. In future, the calibration method should also be probed in intervals with lower plasma densities as the error tends to be higher at lower densities. Moreover, in this study it was not possible, without increasing the error substantially, to use a common photoelectron curve for the calibration of the data of the four spacecraft although they were in a rather similar plasma environment and not being separated more than 24.1 ion inertial lengths. This lack of commonality may be attributed to differences in the photoelectric properties between the spacecraft. Future studies could investigate the effect of including more currents in the current balance equation, depending on the environment of the spacecraft.

A 40 min time interval in the magnetosheath was chosen to validate the potential calibration and to study compressive turbulent fluctuations of the magnetic field and electron density. This analysis implied second-order structure functions expressed as equivalent spectra to examine spectral slopes. The finding that there is a direct transition from the (1/f) regime to the (-8/3) spectral slope with no inertial range (-5/3 slope) in between is consistent with other studies, e.g., Chhiber et al. (2018). Analysis of magnetic field and electron density fluctuations suggests sub-ion scale intermittency in the magnetosheath. The intermittency is a sign for coherent structures that contribute to heating and dissipation in the magnetosheath (Osman et al., 2012; Wu et al., 2013). The magnetic field was transformed into mean-field coordinates, and it can be seen that the power of the structure-function of the parallel, compressive field component is higher than the transverse components, suggesting more intermittency.

A comparison of single- and multi-spacecraft statistics assuming the Taylor frozen-in approximation is made. There seems to be a better agreement between single and multi-spacecraft magnetic field data at large scales than an smaller ones. This suggests higher anisotropies at smaller scales. Nevertheless, it is unclear whether such anisotropies can be found by comparing single- and multi-spacecraft electron density data. More studies in the magnteosheath using multi-spacecraft data should be conducted, potentially using spacecraft potential calibration methods to obtain high-resolution plasma data and investigate turbulent fluctuations down to the smallest scales. Multi-spacecraft data are, however, not only important when examining increments and structure functions like in this paper or Chhiber et al. (2018), but also for other methods. Such include the wave telescope technique (Narita et al., 2022) or two spacecraft correlations (Osman & Horbury, 2007) for instance.

Acknowledgments

All the MMS data is available at the MMS Science Data Center at the Laboratory for Atmospheric and Space Physics (LASP) at the University of Colorado, Boulder (`https://lasp.colorado.edu/mms/sdc/public/`). We want to thank all the MMS instrument teams as well as the SDC team for providing the already processed measurement data. Thank you also for the work done by the SPEDAS team in enabling easy access and plotting methods for the MMS data. This work was supported by the Austrian Research Promotion Agency (FFG): 873685.

References

Alexandrova, O. (2008, February). Solar wind vs magnetosheath turbulence and Alfvén vortices. *Nonlinear Processes in Geophysics*, *15*(1), 95-108. doi: 10.5194/npg-15-95-2008

Andriopoulou, M., Nakamura, R., Torkar, K., Baumjohann, W., & Hoelzl, B. (2015). Deriving plasma densities in tenuous plasma regions, with the spacecraft potential under active control. *Journal of Geophysical Research: Space Physics*, *120*(11), 9594–9616.

Andriopoulou, M., Nakamura, R., Torkar, K., Baumjohann, W., Torbert, R. B., Lindqvist, P. A., ... Russell, C. T. (2016, May). Study of the spacecraft potential under active control and plasma density estimates during the MMS commissioning phase. *Geophysical Research Letters*, *43*(10), 4858-4864. doi: 10.1002/2016GL068529

Andriopoulou, M., Nakamura, R., Wellenzohn, S., Torkar, K., Baumjohann, W., Torbert, R. B., . . . Burch, J. L. (2018). Plasma density estimates from spacecraft potential using mms observations in the dayside magnetosphere. *Journal of Geophysical Research: Space Physics*, *123*(4), 2620–2629.

Baker, D., Riesberg, L., Pankratz, C., Panneton, R., Giles, B., Wilder, F., & Ergun, R. (2016). Magnetospheric multiscale instrument suite operations and data system. *Space Science Reviews*, *199*(1-4), 545–575.

Balcon, N., Payan, D., Belhaj, M., Tondu, T., & Inguimbert, V. (2011). Secondary electron emission on space materials: Evaluation of the total secondary electron yield from surface potential measurements. *IEEE Transactions on Plasma Science*, *40*(2), 282–290.

Bandyopadhyay, R., Matthaeus, W. H., Chasapis, A., Russell, C. T., Strangeway, R. J., Torbert, R. B., . . . Burch, J. L. (2020). Direct measurement of the solar-wind taylor microscale using mms turbulence campaign data. *The Astrophysical Journal*, *899*(1), 63.

Borovsky, J. E., & Gary, S. P. (2014, July). How important are the alpha-proton relative drift and the electron heat flux for the proton heating of the solar wind in the inner heliosphere? *Journal of Geophysical Research (Space Physics)*, *119*(7), 5210-5219. doi: 10.1002/2014JA019758

Bruno, R. (2019, May). Intermittency in Solar Wind Turbulence From Fluid to Kinetic Scales. *Earth and Space Science*, *6*(5), 656-672. doi: 10.1029/2018EA000535

Bruno, R., & Carbone, V. (2013, May). The Solar Wind as a Turbulence Laboratory. *Living Reviews in Solar Physics*, *10*(1), 2. doi: 10.12942/lrsp-2013-2

Burch, J., Moore, T., Torbert, R., & Giles, B. (2016). Magnetospheric multiscale overview and science objectives. *Space Science Reviews*, *199*(1-4), 5–21.

Chasapis, A., Matthaeus, W. H., Bandyopadhyay, R., Chhiber, R., Ahmadi, N., Ergun, R. E., . . . Burch, J. L. (2020, 11). Scaling and anisotropy of solar wind turbulence at kinetic scales during the MMS turbulence campaign. *The Astrophysical Journal*, *903*(2), 127. Retrieved from `https://doi.org/10.3847/1538-4357/abb948` doi: 10.3847/1538-4357/abb948

Chasapis, A., Matthaeus, W. H., Parashar, T. N., Le Contel, O., Retinò, A., Breuillard, H., . . . Saito, Y. (2017, February). Electron Heating at Kinetic Scales in Magnetosheath Turbulence. *The Astrophysical Journal*, *836*(2), 247. doi: 10.3847/1538-4357/836/2/247

Chhiber, R., Chasapis, A., Bandyopadhyay, R., Parashar, T. N., Matthaeus, W. H., Maruca, B. A., . . . Gershman, D. J. (2018, December). Higher-Order Turbulence Statistics in the Earth's Magnetosheath and the Solar Wind Using Magnetospheric Multiscale Observations. *Journal of Geophysical Research (Space Physics)*, *123*(12), 9941-9954. doi: 10.1029/2018JA025768

Czaykowska, A., Bauer, T., Treumann, R., & Baumjohann, W. (2001). Magnetic field fluctuations across the earth's bow shock. In *Annales geophysicae* (Vol. 19, pp. 275–287).

Dudok de Wit, T., Alexandrova, O., Furno, I., Sorriso-Valvo, L., & Zimbardo, G. (2013, October). Methods for Characterising Microphysical Processes in Plasmas. *Space Science Reviews*, *178*(2-4), 665-693. doi: 10.1007/s11214-013-9974-9

Fränz, M., & Harper, D. (2002). Heliospheric coordinate systems. *Planetary and Space Science*, *50*(2), 217–233.

Frisch, U. (1995). *Turbulence. The legacy of A.N. Kolmogorov.*

Garner, R. (2019, 3). *Discovering Bonus Science With NASA's Magnetospheric Multiscale Spacecraft.* `https://www.nasa.gov/feature/goddard/2019/discovering-bonus-science-with-nasa-s-magnetospheric-multiscale-spacecraft`. (Accessed: 2021-04-09)

Graham, D. B., Vaivads, A., Khotyaintsev, Y. V., Eriksson, A. I., André, M., Malaspina, D. M., . . . Plaschke, F. (2018, September). Enhanced Escape of Spacecraft Photoelectrons Caused by Langmuir and Upper Hybrid Waves. *Journal of Geophysical Research (Space Physics)*, *123*(9), 7534-7553. doi: 10.1029/2018JA025874

Kiyani, K., Chapman, S. C., & Hnat, B. (2006, 11). Extracting the scaling exponents of a self-affine, non-gaussian process from a finite-length time series. *Phys. Rev. E*, *74*, 051122. Retrieved from `https://link.aps.org/doi/10.1103/PhysRevE.74.051122` doi: 10.1103/PhysRevE.74.051122

Kiyani, K. H., Osman, K. T., & Chapman, S. C. (2015). *Dissipation and heating in solar wind turbulence: from the macro to the micro and back again.* The Royal Society Publishing.

Klein, K. G., Alexandrova, O., Bookbinder, J., Caprioli, D., Case, A. W., Chandran, B. D. G., ... Whittlesey, P. (2019, March). [Plasma 2020 Decadal] Multipoint Measurements of the Solar Wind: A Proposed Advance for Studying Magnetized Turbulence. *arXiv e-prints*, arXiv:1903.05740.

Kolmogorov, A. (1941, January). The Local Structure of Turbulence in Incompressible Viscous Fluid for Very Large Reynolds' Numbers. *Akademiia Nauk SSSR Doklady*, *30*, 301-305.

Lindqvist, P. A., Olsson, G., Torbert, R. B., King, B., Granoff, M., Rau, D., ... Tucker, S. (2016, March). The Spin-Plane Double Probe Electric Field Instrument for MMS. *Space Science Reviews*, *199*(1-4), 137-165. doi: 10.1007/s11214-014-0116-9

Macek, W. M., Krasińska, A., Silveira, M. V. D., Sibeck, D. G., Wawrzaszek, A., Burch, J. L., & Russell, C. T. (2018, September). Magnetospheric Multiscale Observations of Turbulence in the Magnetosheath on Kinetic Scales. *The Astrophysical Journal Letters*, *864*(2), L29. doi: 10.3847/2041-8213/aad9a8

Markwardt, C. B. (2009). Non-linear least squares fitting in idl with mpfit. *arXiv preprint arXiv:0902.2850*.

Matthaeus, W. H., Dasso, S., Weygand, J. M., Milano, L. J., Smith, C. W., & Kivelson, M. G. (2005, 12). Spatial correlation of solar-wind turbulence from two-point measurements. *Phys. Rev. Lett.*, *95*, 231101. Retrieved from `https://link.aps.org/doi/10.1103/PhysRevLett.95.231101` doi: 10.1103/PhysRevLett.95.231101

Matthaeus, W. H., Wan, M., Servidio, S., Greco, A., Osman, K. T., Oughton, S., & Dmitruk, P. (2015, April). Intermittency, nonlinear dynamics and dissipation in the solar wind and astrophysical plasmas. *Philosophical Transactions of the Royal Society of London Series A*, *373*(2041), 20140154-20140154. doi: 10.1098/rsta.2014.0154

Mott-Smith, H. M., & Langmuir, I. (1926). The theory of collectors in gaseous discharges. *Physical review*, *28*(4), 727.

Nakagawa, T., Ishii, T., Tsuruda, K., Hayakawa, H., & Mukai, T. (2000, April). Net current density of photoelectrons emitted from the surface of the GEOTAIL spacecraft. *Earth, Planets and Space*, *52*, 283-292. doi: 10.1186/BF03351637

Nakamura, R., Torkar, K., Andriopoulou, M., Jeszenszky, H., Escoubet, C., Cipriani, F., ... others (2017). Initial results from the active spacecraft potential control onboard magnetospheric multiscale mission. *IEEE Transactions on Plasma Science*, *45*(8), 1847–1852.

Narita, Y., Gary, S. P., Saito, S., Glassmeier, K.-H., & Motschmann, U. (2011). Dispersion relation analysis of solar wind turbulence. *Geophysical Research Letters*, *38*(5). Retrieved from `https://agupubs.onlinelibrary.wiley.com/doi/abs/10.1029/2010GL046588` doi: https://doi.org/10.1029/2010GL046588

Narita, Y., Glassmeier, K. H., & Motschmann, U. (2022, February). The Wave Telescope Technique. *Journal of Geophysical Research (Space Physics)*, *127*(2), e30165. doi: 10.1029/2021JA030165

Osman, K. T., & Horbury, T. S. (2007, January). Multispacecraft Measurement of

Anisotropic Correlation Functions in Solar Wind Turbulence. *The Astrophysical Journal*, *654*(1), L103-L106. doi: 10.1086/510906
Osman, K. T., Matthaeus, W. H., Wan, M., & Rappazzo, A. F. (2012, 6). Intermittency and local heating in the solar wind. *Phys. Rev. Lett.*, *108*, 261102. Retrieved from https://link.aps.org/doi/10.1103/PhysRevLett.108.261102 doi: 10.1103/PhysRevLett.108.261102
Oughton, S., & Matthaeus, W. H. (2020, July). Critical Balance and the Physics of Magnetohydrodynamic Turbulence. *The Astrophysical Journal*, *897*(1), 37. doi: 10.3847/1538-4357/ab8f2a
Oughton, S., Matthaeus, W. H., Wan, M., & Osman, K. T. (2015). Anisotropy in solar wind plasma turbulence. *Philosophical Transactions of the Royal Society A: Mathematical, Physical and Engineering Sciences*, *373*(2041), 20140152. Retrieved from https://royalsocietypublishing.org/doi/abs/10.1098/rsta.2014.0152 doi: 10.1098/rsta.2014.0152
Pedersen, A. (1995). Solar wind and magnetosphere plasma diagnostics by spacecraft electrostatic potential measurements. In *Annales geophysicae* (Vol. 13, pp. 118–129).
Pedersen, A., Cattell, C. A., Fälthammar, C. G., Formisano, V., Lindqvist, P. A., Mozer, F., & Torbert, R. (1984, March). Quasistatic electric field measurements with spherical double probes on the GEOS and ISEE satellites. *Space Science Reviews*, *37*(3-4), 269-312. doi: 10.1007/BF00226365
Pedersen, A., Décréau, P., Escoubet, C. P., Gustafsson, G., Laakso, H., Lindqvist, P. A., . . . Vaivads, A. (2001, October). Four-point high time resolution information on electron densities by the electric field experiments (EFW) on Cluster. *Annales Geophysicae*, *19*(10), 1483-1489. doi: 10.5194/angeo-19-1483-2001
Pedersen, A., Lybekk, B., André, M., Eriksson, A., Masson, A., Mozer, F. S., . . . Whipple, E. (2008, July). Electron density estimations derived from spacecraft potential measurements on Cluster in tenuous plasma regions. *Journal of Geophysical Research (Space Physics)*, *113*(A7), A07S33. doi: 10.1029/2007JA012636
Perrone, D., Stansby, D., Horbury, T. S., & Matteini, L. (2019, March). Radial evolution of the solar wind in pure high-speed streams: HELIOS revised observations. *Monthly Notices of the Royal Astronomical Society*, *483*(3), 3730-3737. doi: 10.1093/mnras/sty3348
Pollock, C., Moore, T., Jacques, A., Burch, J., Gliese, U., Saito, Y., . . . others (2016). Fast plasma investigation for magnetospheric multiscale. *Space Science Reviews*, *199*(1-4), 331–406.
Roberts, O. W., Alexandrova, O., Sorriso-Valvo, L., Vörös, Z., Nakamura, R., Fischer, D., . . . Yearby, K. (2022). Scale-dependent kurtosis of magnetic field fluctuations in the solar wind: A multi-scale study with cluster 2003–2015. *Journal of Geophysical Research: Space Physics*, *127*(9), e2021JA029483. Retrieved from https://agupubs.onlinelibrary.wiley.com/doi/abs/10.1029/2021JA029483 (e2021JA029483 2021JA029483) doi: https://doi.org/10.1029/2021JA029483
Roberts, O. W., Li, X., & Jeska, L. (2015, 3). A STATISTICAL STUDY OF THE SOLAR WIND TURBULENCE AT ION KINETIC SCALES USING THEK-FILTERING TECHNIQUE AND CLUSTER DATA. *The Astrophysical Journal*, *802*(1), 2. Retrieved from https://doi.org/10.1088/0004-637x/802/1/2 doi: 10.1088/0004-637x/802/1/2
Roberts, O. W., Li, X., & Li, B. (2013, 5). KINETIC PLASMA TURBULENCE IN THE FAST SOLAR WIND MEASURED BYCLUSTER. *The Astrophysical Journal*, *769*(1), 58. Retrieved from https://doi.org/10.1088/0004-637x/769/1/58 doi: 10.1088/0004-637x/769/1/58
Roberts, O. W., Nakamura, R., Torkar, K., Graham, D. B., Gershman, D. J.,

Holmes, J. C., … Giles, B. L. (2020, September). Estimation of the Electron Density From Spacecraft Potential During High-Frequency Electric Field Fluctuations. *Journal of Geophysical Research (Space Physics)*, *125*(9), e27854. doi: 10.1029/2020JA027854

Roberts, O. W., Nakamura, R., Torkar, K., Narita, Y., Holmes, J. C., Vörös, Z., … others (2020). Sub-ion scale compressive turbulence in the solar wind: Mms spacecraft potential observations. *The Astrophysical Journal Supplement Series*, *250*(2), 35.

Roberts, O. W., Narita, Y., Li, X., Escoubet, C. P., & Laakso, H. (2017, July). Multipoint analysis of compressive fluctuations in the fast and slow solar wind. *Journal of Geophysical Research (Space Physics)*, *122*(7), 6940-6963. doi: 10.1002/2016JA023552

Russell, C. T., Anderson, B. J., Baumjohann, W., Bromund, K. R., Dearborn, D., Fischer, D., … Richter, I. (2016, March). The Magnetospheric Multiscale Magnetometers. *Space Science Reviews*, *199*(1-4), 189-256. doi: 10.1007/s11214-014-0057-3

Taylor, G. I. (1938). The spectrum of turbulence. *Proceedings of the Royal Society of London. Series A-Mathematical and Physical Sciences*, *164*(919), 476–490.

Torkar, K., Nakamura, R., & Andriopoulou, M. (2015, September). Interdependencies Between the Actively Controlled Cluster Spacecraft Potential, Ambient Plasma, and Electric Field Measurements. *IEEE Transactions on Plasma Science*, *43*(9), 3054-3063. doi: 10.1109/TPS.2015.2422733

Torkar, K., Nakamura, R., Andriopoulou, M., Giles, B. L., Jeszenszky, H., Khotyaintsev, Y. V., … Torbert, R. B. (2017, December). Influence of the Ambient Electric Field on Measurements of the Actively Controlled Spacecraft Potential by MMS. *Journal of Geophysical Research (Space Physics)*, *122*(12), 12,019-12,030. doi: 10.1002/2017JA024724

Torkar, K., Nakamura, R., Tajmar, M., Scharlemann, C., Jeszenszky, H., Laky, G., … Svenes, K. (2016). Active spacecraft potential control investigation. *Space Science Reviews*, *199*(1-4), 515–544.

Torkar, K., Nakamura, R., Wellenzohn, S., Jeszenszky, H., Torbert, R. B., Lindqvist, P. A., … Giles, B. L. (2019, August). Improved Determination of Plasma Density Based on Spacecraft Potential of the Magnetospheric Multiscale Mission Under Active Potential Control. *IEEE Transactions on Plasma Science*, *47*(8), 3636-3647. doi: 10.1109/TPS.2019.2911425

Williams, L. L., Zank, G. P., & Matthaeus, W. H. (1995, September). Dissipation of pickup-induced waves: A solar wind temperature increase in the outer heliosphere? *Journal of Geophysical Research*, *100*(A9), 17059-17068. doi: 10.1029/95JA01261

Wu, P., Perri, S., Osman, K., Wan, M., Matthaeus, W. H., Shay, M. A., … Chapman, S. (2013). Intermittent heating in solar wind and kinetic simulations. *The Astrophysical Journal*, *763*(2), L30. Retrieved from `https://doi.org/10.1088/2041-8205/763/2/l30` doi: 10.1088/2041-8205/763/2/l30

Yao, S., He, J. S., Marsch, E., Tu, C. Y., Pedersen, A., Rème, H., & Trotignon, J. G. (2011, February). Multi-scale Anti-correlation Between Electron Density and Magnetic Field Strength in the Solar Wind. *The Astrophysical Journal*, *728*(2), 146. doi: 10.1088/0004-637X/728/2/146

Figure 1.

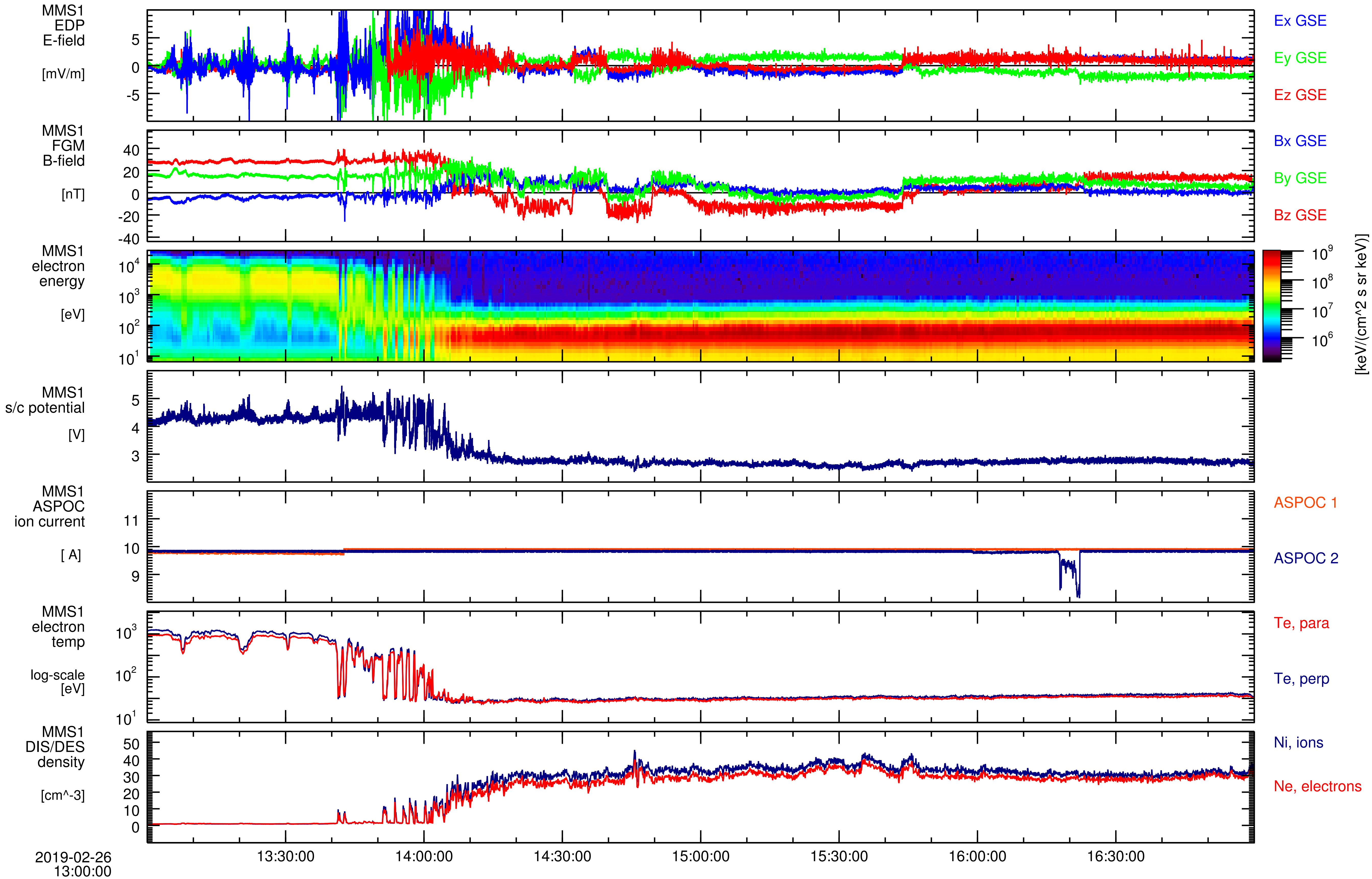
MMS1
EDP
E-field
[mV/m]
Ex GSE
Ey GSE
Ez GSE
MMS1
FGM
B-field
[nT]
Bx GSE
By GSE
Bz GSE
MMS1
electron
energy
[eV]
[keV/(cm^2 s sr keV)]
MMS1
s/c potential
[V]
MMS1
ASPOC
ion current
[A]
ASPOC 1
ASPOC 2
MMS1
electron
temp
log-scale
[eV]
Te, para
Te, perp
MMS1
DIS/DES
density
[cm^-3]
Ni, ions
Ne, electrons
2019-02-26
13:00:00
13:30:00
14:00:00
14:30:00
15:00:00
15:30:00
16:00:00
16:30:00

Figure 2.

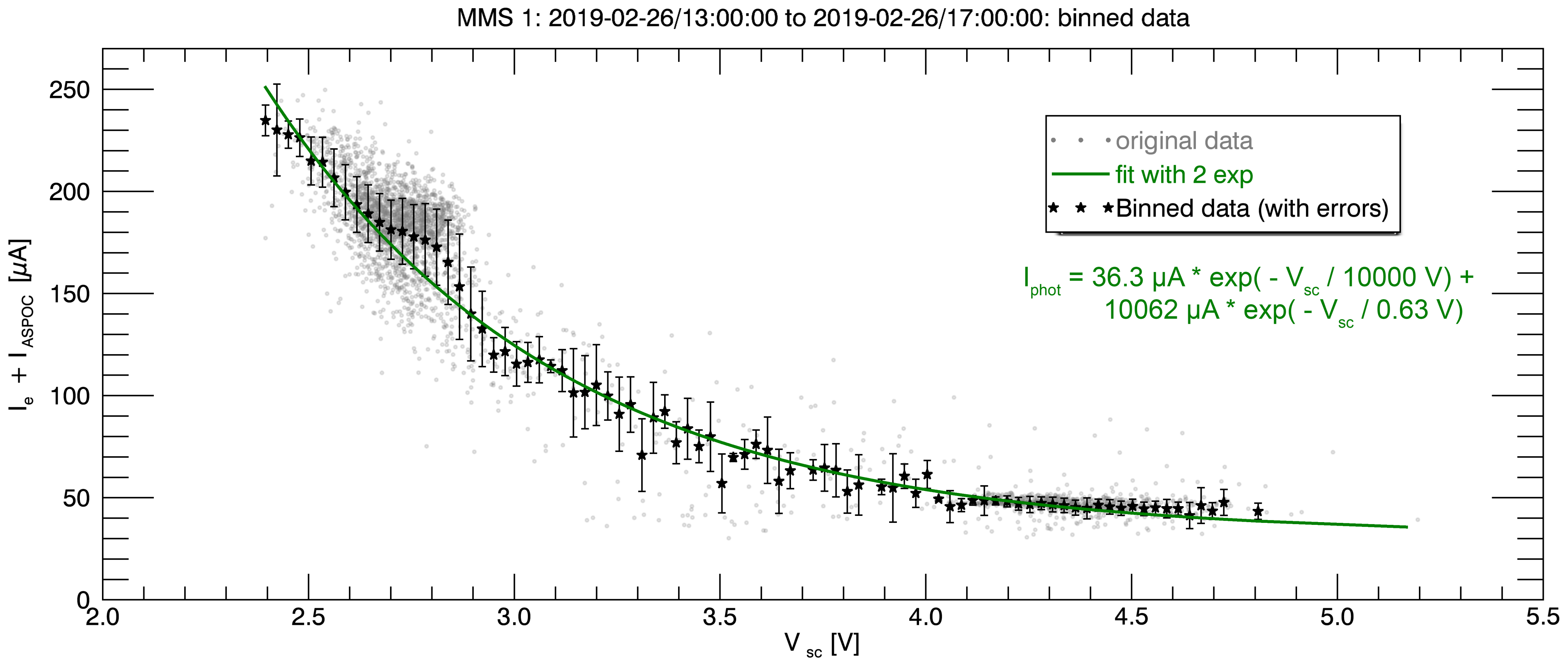

MMS 1: 2019-02-26/13:00:00 to 2019-02-26/17:00:00: binned data
original data
fit with 2 exp
Binned data (with errors)
I_phot = 36.3 μA * exp(- V_sc / 10000 V) +
10062 μA * exp(- V_sc / 0.63 V)
I_e + I_ASPOC [μA]
V_sc [V]
0
50
100
150
200
250
2.0
2.5
3.0
3.5
4.0
4.5
5.0
5.5

Figure 3.

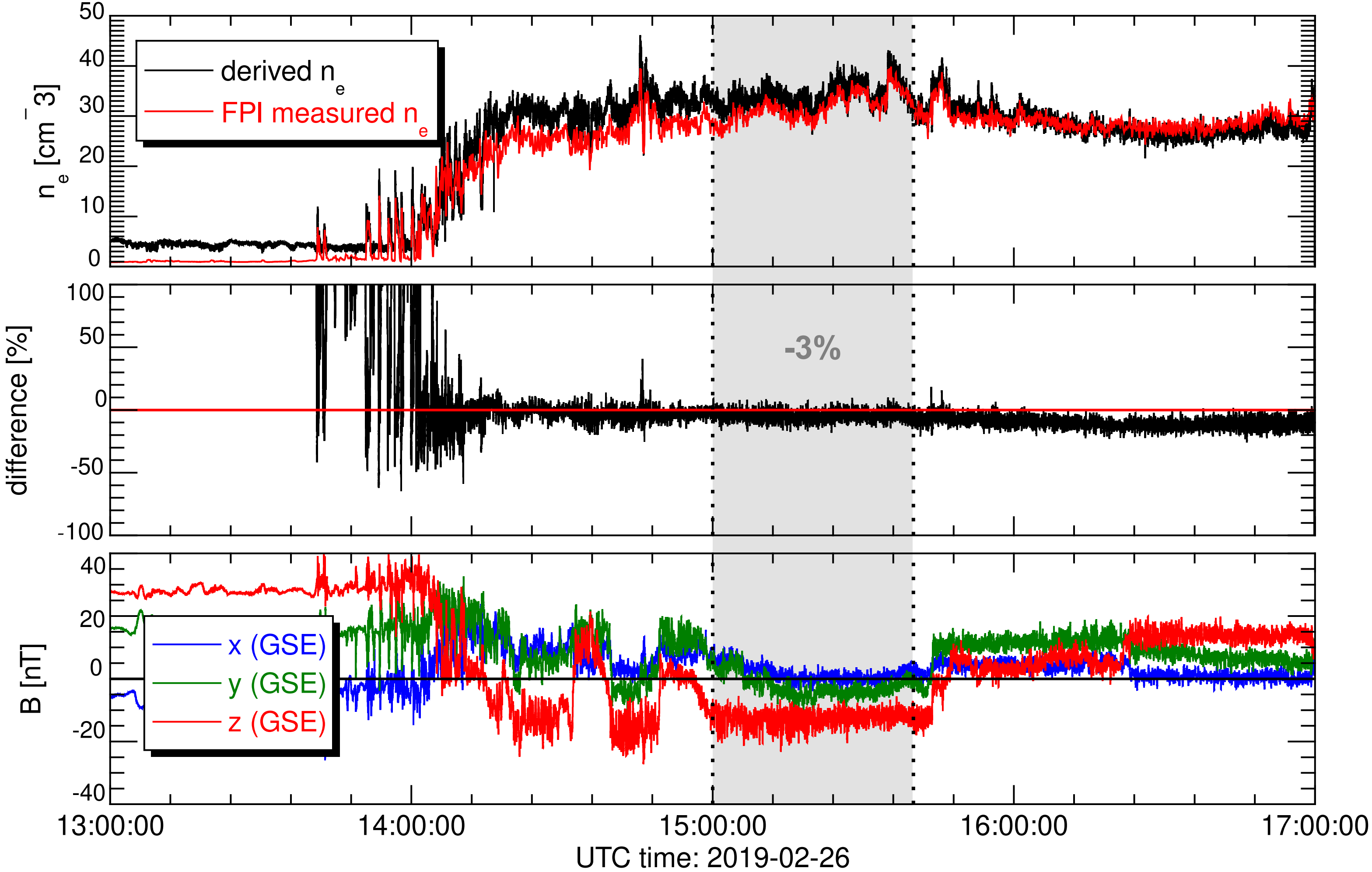

derived n_e
FPI measured n_e
n_e [cm^{-3}]
50
40
30
20
10
0
difference [%]
100
50
0
-50
-100
-3%
B [nT]
x (GSE)
y (GSE)
z (GSE)
40
20
0
-20
-40
13:00:00
14:00:00
15:00:00
16:00:00
17:00:00
UTC time: 2019-02-26

Figure 4.

(a)
(b)
(c)
mms1
mms2
mms3
mms4
V_{sw}
B_0
Y (GSE) relative to MMS 1 [km]
X (GSE) relative to MMS 1 [km]
Z (GSE) relative to MMS 1 [km]
X (GSE) relative to MMS 1 [km]
Z (GSE) relative to MMS 1 [km]
Y (GSE) relative to MMS 1 [km]

Figure 5.

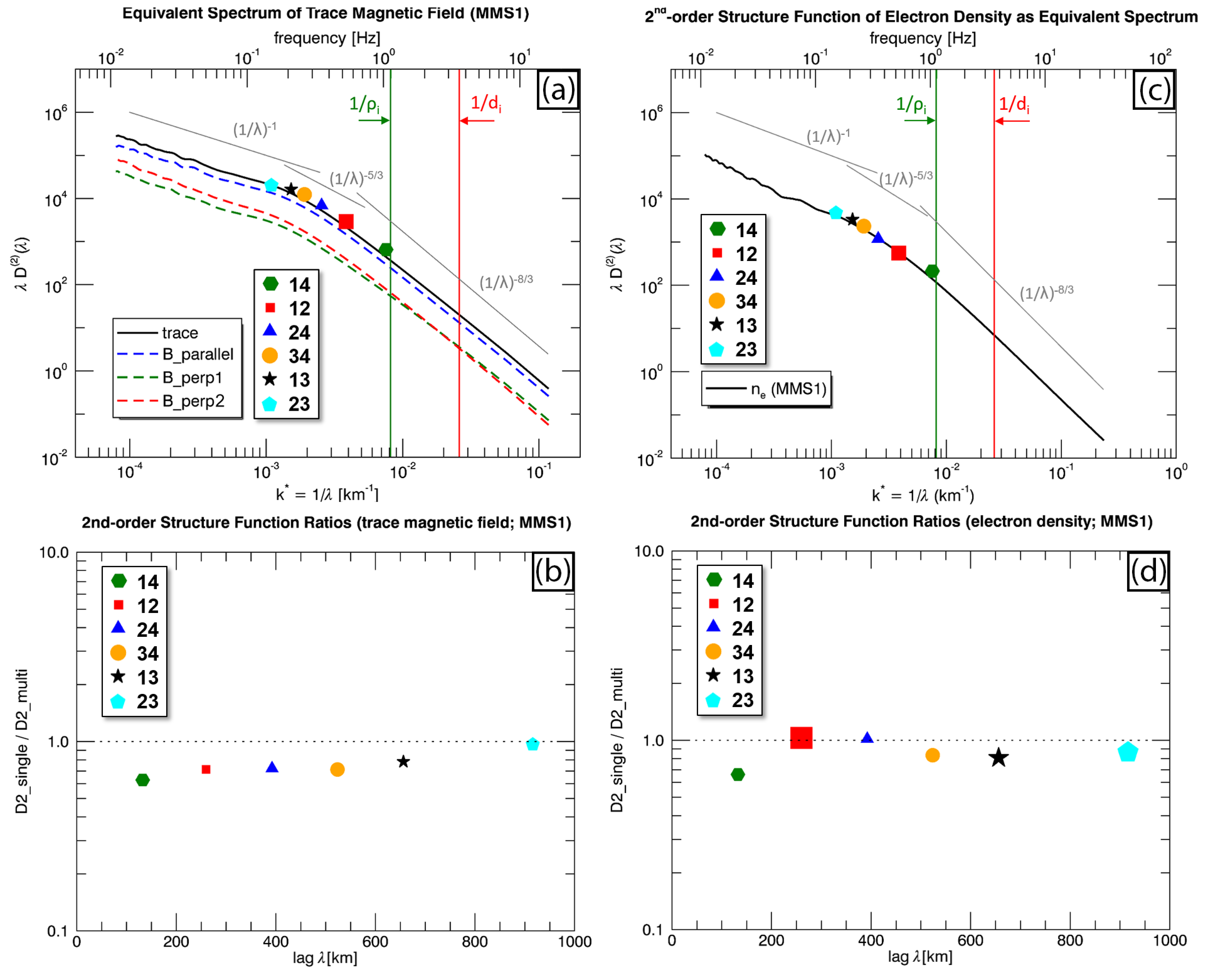

Equivalent Spectrum of Trace Magnetic Field (MMS1)
frequency [Hz]
1/ρ_i
1/d_i
(1/λ)^-1
(1/λ)^-5/3
(1/λ)^-8/3
(a)
λ D^(2)(λ)
k* = 1/λ [km^-1]
trace
B_parallel
B_perp1
B_perp2
14
12
24
34
13
23
2^nd-order Structure Function of Electron Density as Equivalent Spectrum
(c)
n_e (MMS1)
2nd-order Structure Function Ratios (trace magnetic field; MMS1)
(b)
D2_single / D2_multi
lag λ[km]
2nd-order Structure Function Ratios (electron density; MMS1)
(d)